

Characterization and application of the hetero-junction ZnFe₂O₄/TiO₂ for Cr(VI) reduction under visible light

G. Rekhila¹ · M. Trari¹ · Y. Bessekhoud¹

Received: 3 August 2014 / Accepted: 8 September 2015 / Published online: 6 October 2015
© The Author(s) 2015. This article is published with open access at Springerlink.com

Abstract The spinel ZnFe₂O₄ prepared by nitrate route is used as dispersed photons collector capable to sensitize TiO₂ under visible light and to reduce Cr(VI) into trivalent state. The transport properties, optical and photo-electrochemical characterizations are correlated, to build the energetic diagram of the hetero-system ZnFe₂O₄/TiO₂/CrO₄²⁻ solution. A gap of 1.97 eV is obtained for the spinel from the diffuse reflectance. The conduction band of ZnFe₂O₄ (−1.47 V_{SCE}) favors the electrons injection into TiO₂, permitting a physical separation of the charge carriers. The oxidation of oxalic acid by photoholes prevents the corrosion of the spinel. The best configuration ZnFe₂O₄ (75 %)/TiO₂ (25 %) is used to catalyze the downhill reaction (2HCrO₄²⁻ + 3C₂H₄O₄ + 1.5O₂ + 8H⁺ → 2Cr³⁺ + 6CO₂ + 11 H₂O, ΔG° = −557 kcal mol^{−1}). 60 % of Cr(VI) are reduced after 3 h of visible light illumination and the photoactivity follows a first-order kinetic with a half-life of 70 min. The water reduction competes with the HCrO₄²⁻ reduction which is the reason in the regression of the photoactivity; a hydrogen evolution rate of 24 μmol mg^{−1} h^{−1} is obtained.

Keywords Spinel · ZnFe₂O₄ · Hetero-system · Cr(VI) photoreduction · Visible light

Introduction

Solar energy-assisted catalysis on semiconductor materials continue to draw a great interest for the scientific community (Pekakis et al. 2006; Meng et al. 2007; Yaron 2010). It is now well admitted that the photocatalysis is an environmentally friendly alternative able to replace the conventional methods for the water treatment, particularly for low pollutants concentrations (Gumy et al. 2006; Lydakis-Simantiris et al. 2010; Robert and Malato 2002). The activity is untimely dependent on the material and its preparation (Ning et al. 2010; Lifeng et al. 2009) and semiconductors (SCs) employed for such applications are classified into two categories: (1) those characterized by a wide band gap such as TiO₂ and SrTiO₃ which have the advantage of high stability toward the photocorrosion and can be polyvalent in regard to the large panel of applications (Shouai et al. 2008; Jiawen et al. 2011; Chen and Chen 2011). This last aspect is attributed to the electronic bands which are generally of anionic and cationic character, respectively, for the valence (VB) and conduction (CB) bands. However, they absorb only the UV light (λ < 380 nm) and are of little practical use in regard to solar emission, which contain ~5 % of UV irradiation, (2) the second class includes narrow band gap SCs such as CuO and WS₂ which absorb visible light and are attractive for the solar energy conversion (Bessekhoud et al. 2004; Brahimi et al. 2008; Dengwei and Liejin 2007). Unfortunately, this type of SCs is subjected to photocorrosion and is challenged to be stabilized in aqueous electrolytes. The best performance requires a compromise between a negative flat band potential (V_{fb}), a small optical gap (E_g) and a chemical stability.

In this regard, new classes of materials with delafossite “CuBO₂” and spinel “CuB₂O₄” structures have been

✉ M. Trari
solarchemistry@gmail.com

¹ Laboratory of Storage and Valorization of Renewable Energies, Faculty of Chemistry, USTHB, BP 32, 16111 Algiers, Algeria

identified to be promising for the photocatalytic applications (Bessekhouad et al. 2003; Bessekhouad and Trari 2002), B denotes a transition metal. They are successfully applied to generate hydrogen and/or to reduce inorganic pollutants to less harmful forms (Brahimi et al. 2007; Trari et al. 2006). However, their performances remain moderate and suffer from a loss of charge carriers by recombination and low carrier mobility due to the narrow width of d orbital. Noble metals such Pt, Ag and RuO_2 are commonly used to prevent the charge carrier recombination by acting as electron accumulators which facilitate the electron transfer owing to their low over-voltages (Soonhyun and Soo-Keun 2009; Lou et al. 2011; Socha et al. 2006). However, these materials are costly but can be easily recovered after use. It is well established now that the photoreduction yield strongly depends on the morphology of the catalyst and large surface areas with nano-sized crystallites are desirable. Accordingly, the oxides are elaborated by chemical routes to decrease the path the electrons have to diffuse to reach the interface.

On the other hand, the photocatalysis is actively applied on single oxides where the yields remain relatively low. In this respect, many hetero-junctions coupling narrow and wide band gap SCs have been developed (Bessekhouad et al. 2004; Brahimi et al. 2008; Dengwei and Liejin 2007; Helaili et al. 2010). The synergy between the properties of each group of materials results in an increase of the performance of composite SCs under illumination. Nevertheless, this strategy can only be efficient if the properties of the narrow band gap SC which acts as photosensitizer are specific.

The aim of this work is to study the physico-chemical properties of the spinel ZnFe_2O_4 to be used in conjunction with TiO_2 (anatase variety). TiO_2 , indispensable for the charge transfer, provides a bridge between the photoelectrons in ZnFe_2O_4 -CB and chromate. Sacrificial agent must be used to preclude the accumulation of photoholes on semiconductor particles. Exploiting the stabilizing properties of oxalic acid, we have achieved an efficient Cr(VI) photoreduction on the hetero-junction $\text{ZnFe}_2\text{O}_4/\text{TiO}_2$. It is helpful to mention that no reaction occurs between oxalic acid and chromate at low concentrations.

Experimental

Materials preparation

Stoichiometric amounts of $\text{Fe}(\text{NO}_3)_3 \cdot 9\text{H}_2\text{O}$ (Merck, 99.5 %) and $\text{Zn}(\text{NO}_3)_2 \cdot 6\text{H}_2\text{O}$ (Merck, 99.5 %) are dissolved in water. The solution is dehydrated and denitrified by slow heating on a magnetic stirring hot plate. The black precipitate is ground in an agate mortar and calcined at

850 °C (18 h) with intermediate regrindings. TiO_2 is prepared by dissolving $\text{Ti}(\text{OC}_3\text{H}_7)_4$ in methanol/ethanol solution with a molar ratio 1:1:10 according to the method described elsewhere (Bessekhouad et al. 2004). The solution is maintained at 75 °C for 3 h after which water is added dropwise into the hot solution. After gelling, the sample is dried and heat-treated at 400 °C (2 h). The temperature is accurately controlled to prevent the irreversible transition to the rutile phase, less active photocatalytically.

Characterization methods and photoactivity

The phases are identified by X-ray diffraction (XRD) using a Philips diffractometer with a monochromated Cu K_α radiation ($\lambda = 1.5405 \text{ \AA}$) in the 2θ range (20° – 100°). The crystallite size (D) is evaluated from the full width at half-maximum B (FWHM) using the relation $\{D = 0.94 \lambda / (B \cos\theta)^{-1}\}$. FTIR analysis is made by mixing ZnFe_2O_4 ($\sim 2 \%$) with spectroscopic grade KBr. The reflectance diffuse spectra are recorded with a Cary 500 UV–Visible spectrophotometer attached to an integrated sphere; BaSO_4 is used as a reference.

The electrical conductivity ZnFe_2O_4 is measured by the two-terminal method, ZnFe_2O_4 is used in the form of sintered pellets (compactness $\sim 75 \%$). The thermo-power S ($=\Delta V/\Delta T$) is determined with a home made equipment. The pellets are electroded with silver paint and enrobed in close fitting glass holders with epoxy resin, leaving a surface of 0.5 cm^2 . Electrochemical measurements are carried out in H_2SO_4 (0.1 M) electrolyte using a “three electrode device”: ZnFe_2O_4 , a large platinum counter electrode and a saturated calomel electrode (SCE). The current density (J) versus potential (V) is recorded with a PGZ 301 potentiostat (Radiometer analytical). The band edges of the oxides are determined from the capacitance measurements at a frequency of 10 kHz. The electrochemical impedance spectroscopy (EIS) is studied at the open circuit potential (OCP = +0.236 V) using small amplitude sine wave with a frequency analyzer in the range (10^{-2} – 10^5 Hz).

The photocatalytic experiments are done in a double-walled borosilicate reactor connected to a thermostated bath allowing a temperature control (25 ± 0.5 °C). The powder (50 mg) of the mixture ($\text{ZnFe}_2\text{O}_4/\text{TiO}_2$) at various percentages is dispersed by magnetic agitation in 50 mL of solution ($\text{HCrO}_4^- + \text{OA}$, pH ~ 3). The chrono-potentiometric profile is measured in the working solution using Pt (Tacussel) as indicator electrode. The mixture is maintained in the dark overnight and irradiated with a tungsten lamp (200 W), providing an intensity of 8.3 mW cm^{-2} . The aliquots are withdrawn at regular time intervals and subjected to a vigorous centrifugation (3000 rpm, 10 min) to separate the solid particles. The progress of the Cr(VI)

reduction is followed by plotting the spectra with a UV–Visible spectrophotometer (Shimadzu 1800, $\lambda_{\text{max}} = 350$ nm). CO₂-free distilled water is used in all experiments.

Results and discussion

Characterization

The nitrate route provides a homogeneous morphology and prevents the formation of segregated phases which act as carrier traps, thereby causing a decrease of the photoactivity. The end product exhibits a brown color, the XRD pattern (Fig. 1) reveals a single phase with good crystallinity. All peaks are assigned to the normal spinel Zn[Fe₂]O₄ crystallizing in a cubic symmetry (space group: Fd3 m) with a lattice constant of 0.8441 nm, in agreement with the JCPDS card No. 22-1012; the main physical properties are given in Table 1. The crystallite size (*D*) evaluated from FWHM averages 40 nm. Assuming spherical and non-porous crystallites, a specific surface area of 30 cm² g⁻¹ (=6/ ρD) is determined; ρ being the experimental density (4.92 g cm⁻³). The FTIR spectrum (Fig. 2) is similar to that given of isotypic spinels (Bessekhouad and Trari 2002). The bands centered at 560 and 451 cm⁻¹ are assigned to Zn²⁺ and Fe³⁺ ions, respectively, in tetrahedral and octahedral sites (Lahmar et al. 2012) while the band at 1630 cm⁻¹ is due to water when the oxide is handled in air.

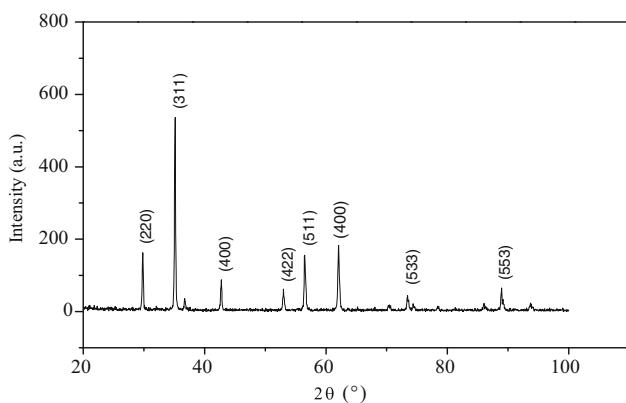


Fig. 1 X-ray diffraction pattern of ZnFe₂O₄ synthesized via sol-gel method

The diffuse reflectance (Fig. 3) is used to determine the optical properties of ZnFe₂O₄. The gap is obtained from the plot $(\alpha h\nu)^n$ versus $h\nu$ where *n* takes the value 1/2 or 2, respectively, for indirect and direct optical transitions, α being the optical absorption coefficient. The extrapolation of the linear part of $(\alpha h\nu)^2$ intercepts the $h\nu$ axis at 1.97 eV and the transition is directly allowed (Fig. 3, inset). The thermal dependence of the electrical conductivity of ZnFe₂O₄ (Fig. 4) is characteristic of a semi-conducting behavior. The data are fitted by an exponential law $\sigma = \sigma_0 \exp(-E_a/RT)$, σ_0 is the pre-exponential factor. The linearization of this equation gives activation energy (*E_a*) of 0.22 eV, suggesting that the conduction occurs by thermal activation of the carrier density. The thermo-power (*S*) is less sensitive to grain boundaries and likely corresponds to the bulk properties. It is positive over the entire temperature range (Fig. 5) which indicates that the majority carriers are holes and confirms a conduction mechanism by small polaron hopping through mixed iron valences. The thermal dependence of *S* is consistent with non-degenerate conductivity and its value implies a density of the order of magnitude of $\sim 10^{20}$ cm⁻³ (see below).

The position of the electronic bands and their widths are imposed by the crystal structure which plays indubitably a crucial role in the photo-electrochemical (PEC) conversion. The flat band potential (*V_{fb}*) is determined under the operating conditions using the Mott–Schottky relation:

$$C^{-2} = \{2/\varepsilon\varepsilon_0N_A\}\{V - V_{fb} - kT/e\} \quad (1)$$

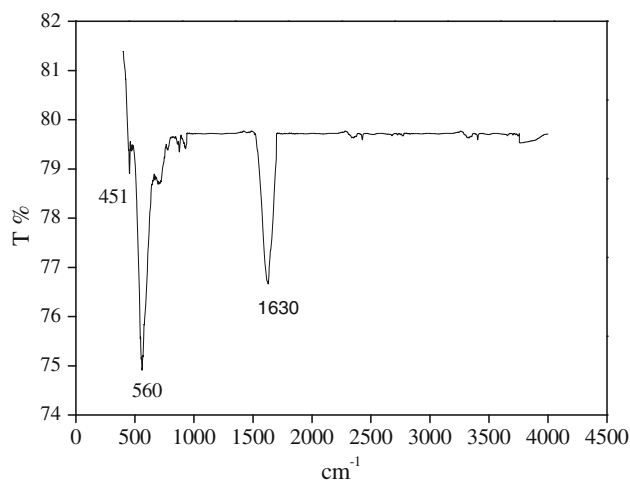


Fig. 2 FT-IR spectrum of ZnFe₂O₄

Table 1 The physical properties of the spinel ZnFe₂O₄ and TiO₂ (anatase polymorph)

| Oxide | Color | Structure | E _g (eV) | E _a (eV) | Type | V _{fb} (V _{SCE}) |
|----------------------------------|-------|-----------|---------------------|---------------------|----------|-------------------------------------|
| ZnFe ₂ O ₄ | Brown | Spinel | 1.97 | 0.22 | <i>p</i> | 0.36 |
| TiO ₂ | White | Anatase | 3.2 | ~0.3 | <i>n</i> | -0.50 (Brahimi et al. 2008) |

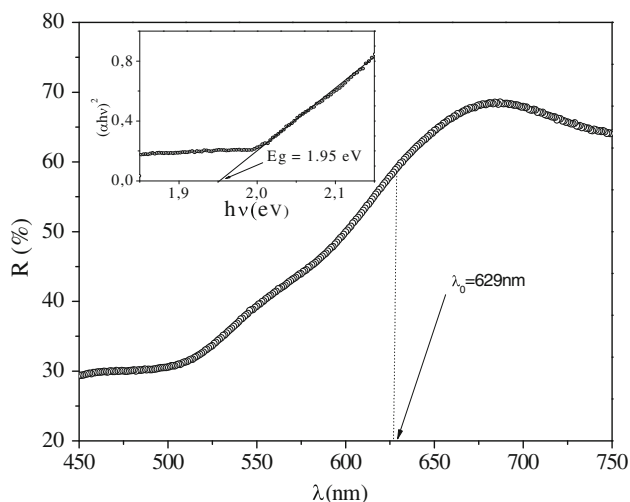


Fig. 3 Diffuse reflectance spectrum of ZnFe_2O_4 . Inset direct band gap transition

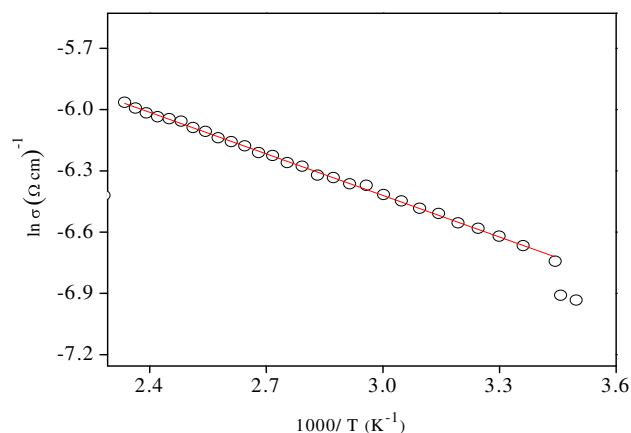


Fig. 4 The thermal dependence of the electrical conductivity of ZnFe_2O_4

The potential V_{fb} (0.361 V) is obtained from the extrapolation of the plot to $C^2 = 0$ (Fig. 6) while the linear part ($C^2 - V$) indicates a holes density N_A ($3 \times 10^{19} \text{ cm}^{-3}$) characteristic of moderately doped SC with a broad depletion width δ (480 nm):

$$\delta = \left(\frac{2\epsilon\epsilon_0(V - V_{fb})}{eN_A} \right)^{0.5} \quad (2)$$

The difference ($V - V_{fb} \sim 0.4 \text{ V}$), used for the calculation of δ , represents the optimal band bending at the interface which prevents the recombination of electron/hole (e^-/h^+) pairs. The potential V_{fb} outlines the energetic position of ZnFe_2O_4 -VB with respect to vacuum:

$$E_{VB} = 4.75 + e V_{fb} + 0.059 (\text{pH} - \text{pH}_{\text{pzpp}}) + E_a \quad (3)$$

pH_{pzpp} is the point of zero zeta potential (≈ 7.30). VB is located at $5.3 \pm 0.1 \text{ eV}$, a value close to that obtained for

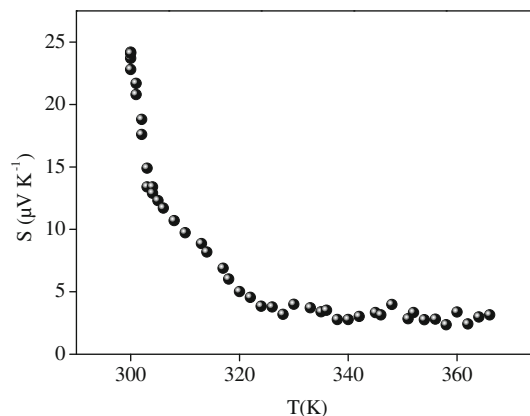


Fig. 5 Thermal dependence of the thermo-power of ZnFe_2O_4

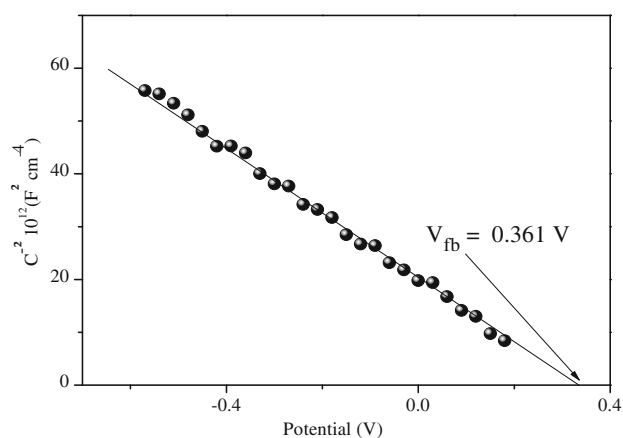


Fig. 6 The Mott-Schottky characteristic of ZnFe_2O_4 plotted in the working solution at a frequency of 10 kHz

iso-structural spinel (Bessekhouad and Trari 2002). This is attractive in the fact that VB is made up of $3d$ orbital, which decreases the optical gap while maintaining the advantage of a high reducing ability of ZnFe_2O_4 -CB. Indeed, the oxygen crystal field splits the orbital Fe^{3+} : $3d^6$ (high spin) by $\sim 2 \text{ eV}$; the transition is of $d-d$ characteristic and involves lower and upper bands of $3d$ orbital.

Photoactivity

A correlation exists between the physico-chemical properties of the spinels and the photoactivity (Nyquist and Kagel 1978). The spinels are small polaron SCs with a low carrier mobility ($\sim 10^{-6} \text{ cm}^2 \text{ V}^{-1} \text{ s}^{-1}$)²¹ due to the narrow of $3d$ orbital, not exceeding 2 eV. Accordingly, the PEC performance should be improved by decreasing the crystallite size until it becomes comparable with the diffusion length of the minority carriers. Hence, it is attractive to

^{Par17} Calculated from the relation $\sigma = e \mu_h N_A$.

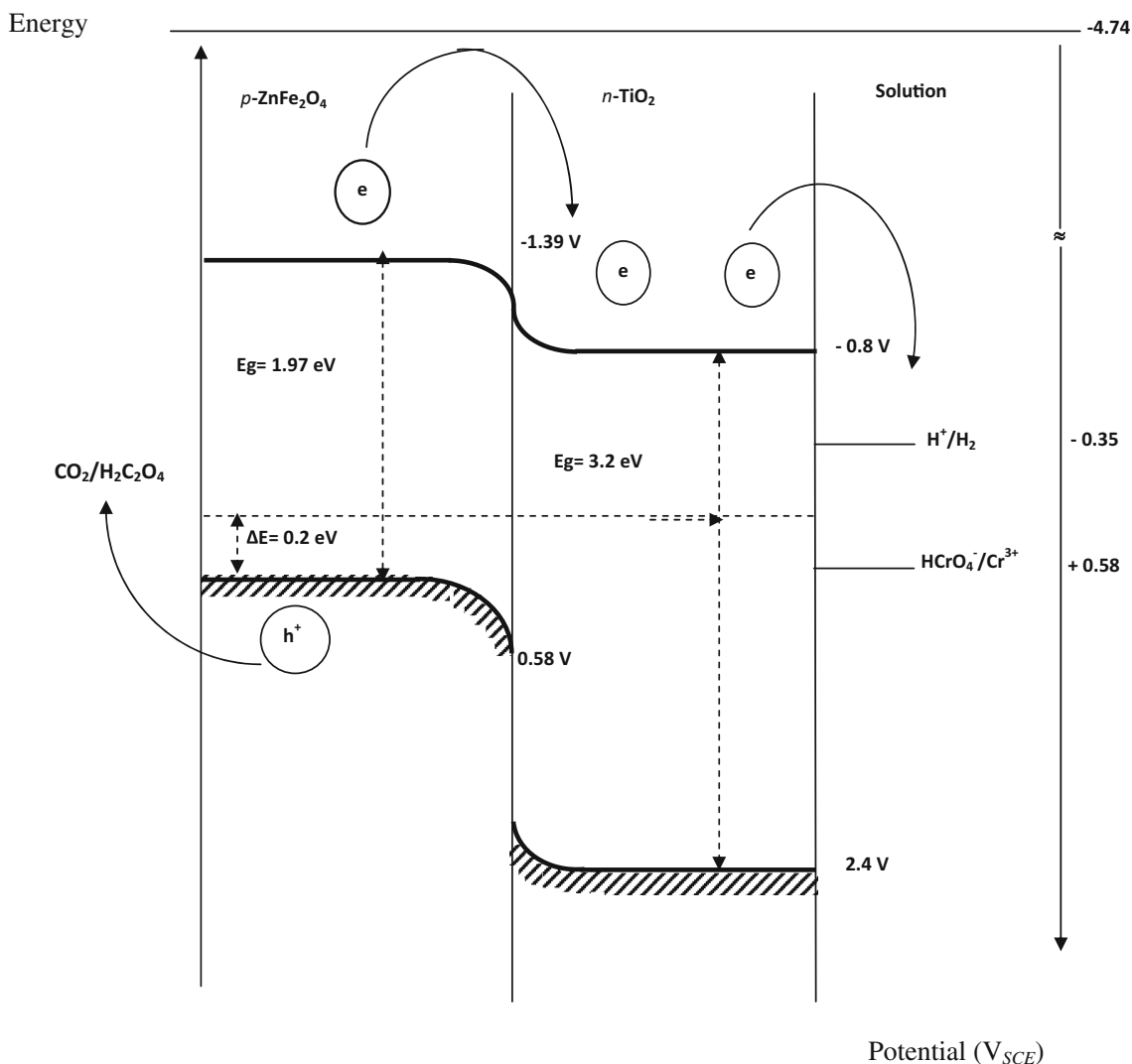


Fig. 7 The energy band diagram of $\text{ZnFe}_2\text{O}_4/\text{TiO}_2/\text{electrolyte}$ junction of the photo-electrochemical cell

prepare the catalyst by nitrate route to reduce the path the electrons have to diffuse to be injected into $\text{TiO}_2\text{-CB}$.

The heterogeneous charge transfer occurs iso-energetically between the semi conductor and redox couple. However, for the junction $\text{ZnFe}_2\text{O}_4/\text{HCrO}_4^-$, the difference ($E_{\text{CB}} - E_{\text{red}}$) is large (~ 1.4 V) for a direct electron exchange and the chromate reduction does not take place (zero photoactivity). In this regard, the hetero-systems have attracted a great attention for favoring the charges separation and harvesting the sunlight and the choice of the wide band gap SC is of primary importance for an acceptable yield. TiO_2 is excited by UV radiation, ruling out the exploitation of the visible light and this makes it unattractive for the solar energy conversion (Kezzim et al. 2011). With an attempt to extend the spectral response toward the visible region and to minimize the loss of ($e^-/$

h^+) pairs, the configuration $p\text{-ZnFe}_2\text{O}_4/n\text{-TiO}_2$ is considered. The physical and PEC characterisations permit to draw the energy diagram (Fig. 7) which predicts from a thermodynamic point of view whether the HCrO_4^- reduction occurs or not. The photoelectrons react with HCrO_4^- via TiO_2 interfacial mechanism. $\text{ZnFe}_2\text{O}_4\text{-CB}$ made up of $3d$ orbital is pH insensitive while $\text{TiO}_2\text{-CB}$ changes usually by 0.06 V pH^{-1} . We have taken advantage of this property and in acidic medium ($\text{pH} \sim 3$) the bands are appropriately adjusted to have an optimal band bending. HCrO_4^- is the dominant specie at low pHs due to the acidity constant ($\text{CrO}_4^{2-} + \text{H}_2\text{O} \rightarrow \text{HCrO}_4^- + \text{OH}^-$, $\text{pK}_a = 6.5$). It is generally an accepted view that the heterogeneous charge transfer involves an adsorption, a precondition for the photocatalysis and before the photocatalytic test, the solution is maintained in the dark

overnight. The HCrO_4^- adsorption on TiO_2 is pH dependent; it follows an anionic type law and is pronounced below p_{zpc} (=6.80), i.e., the pH for which the surface charge of TiO_2 is zero and where the adsorption of OH^- and H_3O^+ balance each other. Per against, in basic medium, the negative charge electrostatically hinders the access of chromate to TiO_2 .

It is worthwhile to outline that no reaction between chromate and oxalic acid occurs since no change in the UV spectrum is observed. Hence, any change in the Cr(VI) concentration is attributed to the photocatalytic process. Figure 8 shows the chrono-potentiometric profile of the powder suspension under illumination, the potential goes to cathodic values, indicating that the reduction of HCrO_4^- takes place. The process starts by the photoactivation of the sensitizer ZnFe_2O_4 upon visible light which results in the generation of (e^-/h^+) pairs. The charge carriers are separated by the electrical field developed at the interface $\text{ZnFe}_2\text{O}_4/\text{TiO}_2$; electrons are injected into $\text{TiO}_2\text{-CB}$ and subsequently transferred to adsorbed HCrO_4^- . In this configuration, the reduction of HCrO_4^- takes place at the solid interface $\text{TiO}_2/\text{electrolyte}$ while the oxidation of oxalic acid occurs concomitantly on ZnFe_2O_4 :

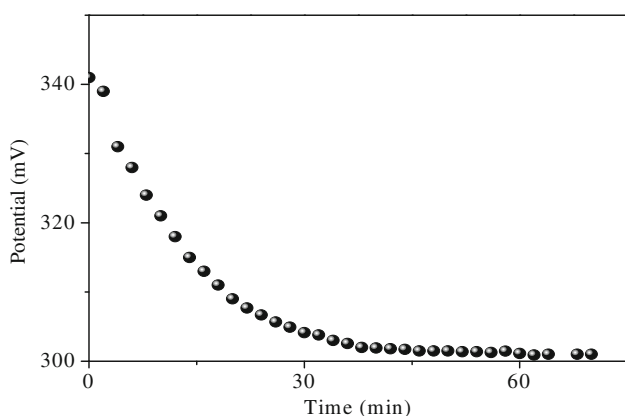
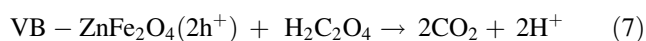
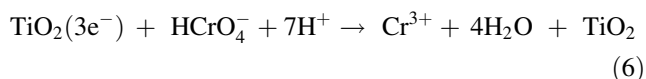
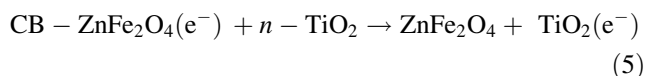
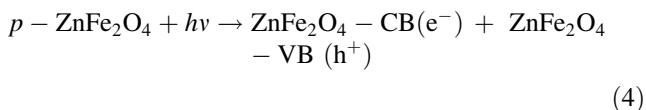


Fig. 8 Chrono-potentiometric curve of Cr(IV) adsorption on ZnFe_2O_4 suspension

The presence of oxalic acid precludes the undesirable corrosion, and favors the charge separation (Sapoval and Hermann 2003). Due to the energy difference between the corresponding conduction bands of both SC_s , an electromotive force is generated, thus inducing an acceleration of the electrons transfer with a diffusion potential (V_D) given by:

$$eV_D = |E_{\text{ZnFe}_2\text{O}_4\text{-CB}} - E_{\text{TiO}_2\text{-CB}}| \quad (9)$$

The optimal ratio between the photons collector “ ZnFe_2O_4 ” and the electrons acceptor “ TiO_2 ” is investigated (Fig. 9) and the best performance occurs for $\text{ZnFe}_2\text{O}_4/\text{TiO}_2$: 75 %/25 with a potential V_D of 0.67 V. ZnFe_2O_4 governs the efficiency and catalyzes the downhill reaction ($\Delta G^\circ = -557 \text{ kcal mol}^{-1}$):

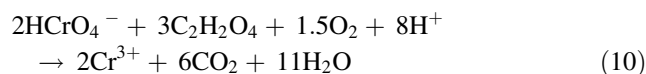


Figure 10a compares the UV–Visible spectra of chromate solutions over illumination time. The decay in absorbance at 350 nm is due to a decrease of HCrO_4^- concentration since no change has been observed in the dark. The absence of additional peak in the spectrum of 4-h illuminated solution is due to the adsorption of Cr^{3+} and which should appear at 300 nm. The plot $\log(\text{HCrO}_4^-)$ –time indicates a first-order reaction with a half-life of 70 min (Fig. 10b). The tendency to saturation observed over time (Fig. 10b, inset) cannot be explained on the basis of optical reasons. Indeed, the absorption of HCrO_4^- solution at low concentration is weak in the visible region; only 5 % of light is absorbed for 1-cm path at 540 nm for 100 ppm. Accordingly, the bending over the curve beyond ~150 min is due to water reduction. This question has already been examined by some of us (Nyquist and Kagel 1978). The HCrO_4^- reduction takes

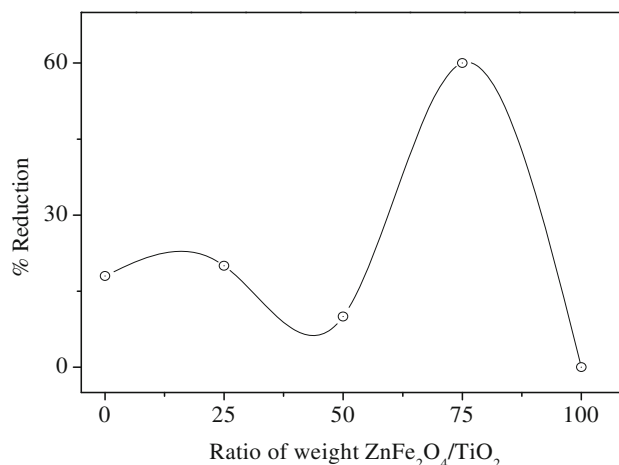


Fig. 9 Influence of the mass ratio ZnFe_2O_4 and TiO_2 on the photo reduction

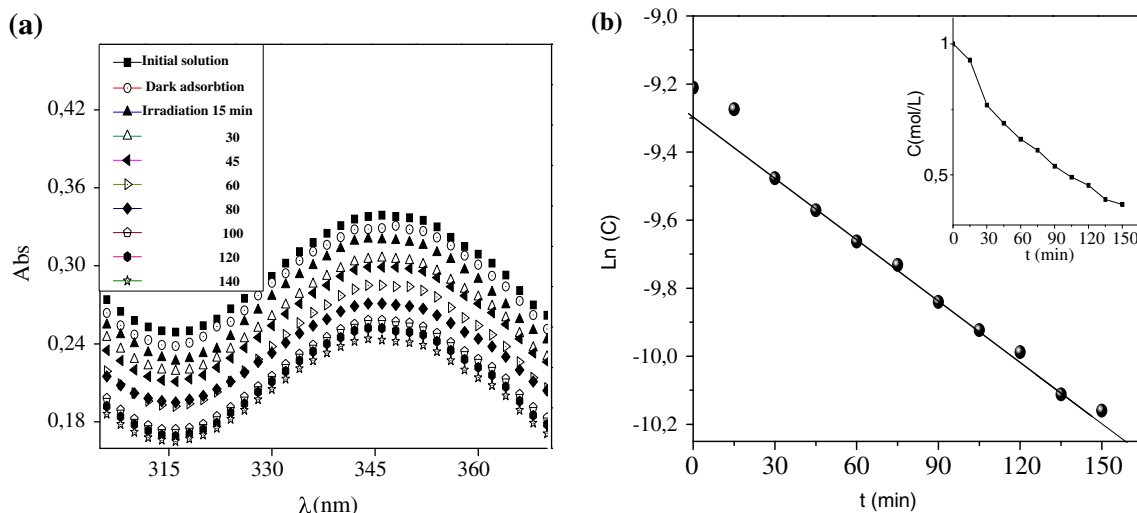


Fig. 10 **a** UV–Visible spectra of ZnFe₂O₄ in aqueous solutions over reaction time. **b** The plot of ln C as function of time. *Inset* photoreduction of chromate on ZnFe₂O₄

place competitively with the H₂ evolution and, therefore, seems the main reason in the regression of the photoactivity (see below Fig. 12). This can be easily understood in terms of energy levels of TiO₂-CB, HCrO⁻ and H₂O. In air-equilibrated suspension, the potential of the couple H₂O/H₂ (~ -0.35 V) is below TiO₂-CB (-0.8 V), yielding a feasible H₂ liberation which contributes for ~ 50 % of the total irradiance.

The electrochemical impedance spectroscopy (EIS) correlates the photocatalytic performance to the morphology of the material and brings insights on the interfacial mechanisms; it is used to quantify the contributions of the bulk and grains boundaries at the junction ZnFe₂O₄/solution. The EIS spectra are plotted at the open circuit potential (OCP = +0.286 V) both in the dark and under illumination. The spectrum exhibits two arcs (Fig. 11) which deviate from an ideal capacitive behavior, thus revealing an apparent constant phase element (CPE):

$$Z = \{Q(j\omega)k\}^{-1} \tag{11}$$

where *Q* is a frequency independent constant, *j* the imaginary number (*j*² = -1), *ω* the angular frequency and *k* the homogeneity factor. Indeed, the centers of the semi-circles are localized below the abscissa axis (*β*₁ and *β*₂, Table 2), indicating a dipolar nature of the spinel with multi relaxation processes and where the electron hopping occurs with a low-potential barrier. The slight offset near the origin is due to the electrolyte resistance *R*_{el} (~ 10 Ω cm²) and remains nearly unchanged under light. As expected for a semi-conducting material, the diameter of the first semicircle (bulk contribution) decreases under light. The illumination increases the ability of dipoles to align along the junction electric field which raises the effective length of dipole (Table 2). The lower polarization resistance of TiO₂ under illumination indicates a decrease of the ohmic drop. The absence of straight line at low

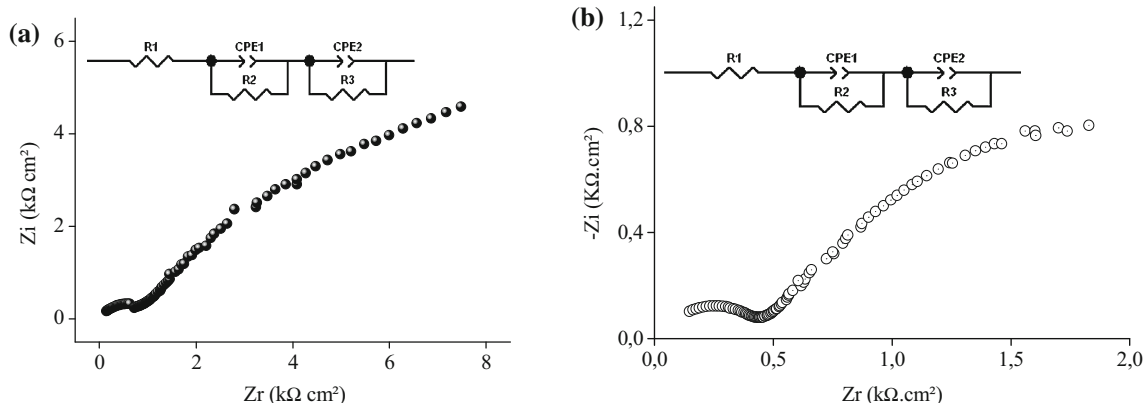
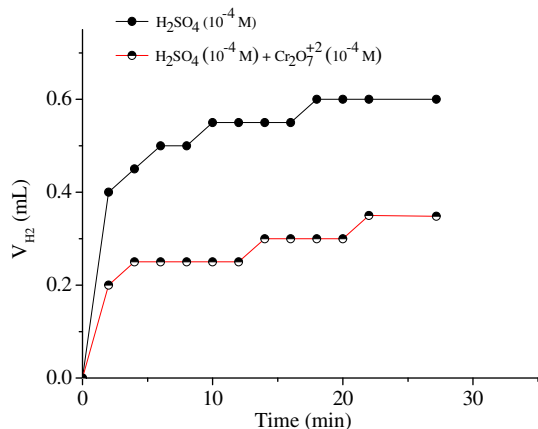


Fig. 11 The Nyquist plots of ZnFe₂O₄ in the chromate solution: **a** in the dark **b** under illumination

Table 2 EIS parameters from the equivalent circuit of ZnFe_2O_4 in Cr(VI) electrolyte

| | R_s ($\Omega \text{ cm}^2$) | R_1 ($\Omega \text{ cm}^2$) | β_1 (degrees) | CPE ₁ (nF/cm ²) | R_2 (Ω) ($\Omega \text{ cm}^2$) | β_2 (degrees) | CPE ₂ ($\mu\text{F}/\text{cm}^2$) | ω_{\min} (Hz) | τ_r (ms) |
|--------------|---------------------------------|---------------------------------|---------------------|--|--|---------------------|--|----------------------|---------------|
| Dark | 9.285 | 1064 | -15.3 | 9.447 | 17,440 | -17.1 | 1.263 | 56.10 | 2.83 |
| Illumination | 11.58 | 487.2 | -17.2 | 8.166 | 3340 | -17.5 | 33.92 | 5.19 | 30.62 |

**Fig. 12** The volume of evolved hydrogen in presence and in absence of chromate

frequencies clearly shows that the process is under kinetic control. The electrical circuit parameters, determined from the experimental data, are given in Fig. 11 (inset) while the EIS parameters are gathered in Table 2. The minimum angular frequency (ν_{\min}) permits the determination of the lifetime of electrons (τ) which increases by a factor of 10 under illumination (Table 2) giving the electrons a higher probability to reach to interface, thus contributing efficiently to the chromate reduction.

Conclusion

This work deals with the development of semiconductors configuration for photocatalytic applications. ZnFe_2O_4 has a conduction band of cationic character with a high reducing ability and acts as photo electrons collector. For this purpose, *d*-type configuration may be used and we successfully prepared the spinel by nitrate route with nanocrystallite sizes. ZnFe_2O_4 is chemically stable, safe and low cost. The transport properties reveal *p*-type conductivity with a small polaron hopping. The optical and photo-electrochemical characteristics allow building the energetic diagram which predicts the electron injection into TiO_2 . The best configuration is obtained with 75 % of ZnFe_2O_4 which favors the charges separation and enhances the photo activity. The reduction obeys to a first-order kinetic with a half-life of 70 min. The bulk resistance R_b of

the spinel decreases under illumination while the higher resistance of the grain boundaries indicates an increase of the barrier potential. The photoelectrons generated in ZnFe_2O_4 are injected to TiO_2 and subsequently transferred to Cr(VI) which is reduced to trivalent state. The saturation over illumination time is due to the competitive water reduction which consumes half of the total photons flux.

Acknowledgments The authors wish to record the assistance of Dr. S. Omeiri in carrying out the EIS measurements. The work was supported by the Faculty of Chemistry (USTHB, Algiers).

Open Access This article is distributed under the terms of the Creative Commons Attribution 4.0 International License (<http://creativecommons.org/licenses/by/4.0/>), which permits unrestricted use, distribution, and reproduction in any medium, provided you give appropriate credit to the original author(s) and the source, provide a link to the Creative Commons license, and indicate if changes were made.

References

- Bessekhouad Y, Trari M (2002) Photocatalytic hydrogen production from suspension of spinel powders AMn_2O_4 (A = Cu and Zn). *Int J Hydrog Energy* 27:357–362
- Bessekhouad Y, Robert D, Weber JV (2003) Synthesis of photocatalytic TiO_2 nanoparticles: optimization of the preparation conditions. *J Photochem Photobiol A* 157:47–53
- Bessekhouad Y, Robert D, Weber JV (2004) $\text{Bi}_2\text{S}_3/\text{TiO}_2$ and CdS/TiO_2 hetero-junctions as an available configuration for photocatalytic degradation of organic pollutant. *J Photochem Photobiol A* 63:569–580
- Brahimi R, Bessekhouad Y, Bouguelia A, Trari M (2007) $\text{CuAlO}_2/\text{TiO}_2$ heterojunction applied to visible light H_2 production. *J Photochem Photobiol A* 186:242–247
- Brahimi R, Bessekhouad Y, Bouguelia A, Trari M (2008) Improvement of eosin visible light degradation using PbS-sensitized TiO_2 . *J Photochem Photobiol A Chem* 194:173–180
- Chen YH, Chen YD (2011) Kinetic study of Cu(II) adsorption on nanosized BaTiO_3 and SrTiO_3 photocatalysts. *J Hazard Mater* 185:168–173
- Dengwei J, Liejin G (2007) WS_2 . *Catal Commun* 8:795–799
- Gumy D, Rincon AG, Hajdu R, Pulgarin C (2006) Solar photocatalysis for detoxification and disinfection of water: different types of suspended and fixed TiO_2 catalysts study. *Sol Energy* 80:1376–1381
- Helaili N, Bessekhouad Y, Bouguelia A, Trari M (2010) *p*- $\text{Cu}_2\text{O}/\text{n-ZnO}$ heterojunction applied to visible light Orange II degradation. *Sol Energy* 84:1187–1192
- Jiawen L, Yue S, Zhonghua L, Shuying L, Jingxiang Z (2011) Photocatalytic hydrogen production from water/methanol solutions over highly ordered Ag-SrTiO_3 nanotube arrays. *Int J Hydrog Energy* 36:5811–5816

- Kezzim A, Nasrallah N, Abdi A, Trari M (2011) Visible light induced hydrogen on the novel hetero-system $\text{CuFe}_2\text{O}_4/\text{TiO}_2$. *Energy Convers Manag* 52:2800–2806
- Lahmar H, Kebir M, Nasrallah N, Trari M (2012) Photocatalytic reduction of Cr(VI) on the new hetero-system $\text{CuCr}_2\text{O}_4/\text{ZnO}$. *J Mol Catal A Chem* 353–354:74–79
- Lifeng C, Yuansheng W, Mutong NC Guoxin, Cheng Y (2009) Synthesis and visible light photocatalysis of Fe-doped TiO_2 mesoporous layers deposited on hollow glass microbeads. *J Solid State Chem* 182:2785–2790
- Lou S, Xiao Y, Yang L, Liu C, Su F, Li Y, Cai Q, Zeng G (2011) Simultaneous detoxification of hexavalent chromium and acid orange 7 by a novel Au/TiO_2 heterojunction composite nanotube arrays. *Sep Purif Technol* 79:85–91
- Lydakis-Simantiris N, Riga D, Katsivela E, Mantzavinos D, Xekoukoulotakis NP (2010) Disinfection of spring water and secondary treated municipal wastewater by TiO_2 photocatalysis. *Desalination* 250:351–355
- Meng N, Leung MKH, Dennis YCL, Sumathy K (2007) A review and recent developments in photocatalytic water-splitting using TiO_2 for hydrogen production. *Renew Sustain Energy* 11:401–425
- Ning X, Zhonghua L, Jiawen L, Yuan G (2010) A facile template-free method for preparing bi-phase TiO_2 nanowire arrays with high photocatalytic activity. *Mater Lett* 64:1776–1778
- Nyquist RA, Kagel RO (1971) Infrared spectra of inorganic compounds ($3800\text{--}45\text{ cm}^{-1}$). Academic Press, New York
- Pekakis AP, Xekoukoulotakis PN, Mantzavinos D (2006) Treatment of textile dye house wastewater by TiO_2 photocatalysis. *Water Res* 40:1276–1286
- Robert D, Malato S (2002) Solar TiO_2 photocatalysis: a clean process for water detoxification. *Sci Total Environ* 291:85–97
- Sapoval B, Hermann C (2003) *Physics of semiconductors*. Springer, Berlin
- Shouai F, Jianghong Z, Zhenping Z (2008) Kinetically restraining aggregation of ZnS nanocrystals and the effect on photocatalysis. *Mater Sci Eng B* 150:116–120
- Socha A, Chrzescijanska E, Kusmierek E (2006) Photoelectrochemical treatment of 1-amino-8-hydroxynaphthalene-3,6-disulphonic acid at electrode covered with $\text{TiO}_2/\text{RuO}_2$. *Dye Pigment* 71:10–18
- Soonhyun K, Soo-Keun L (2009) Visible light-induced photocatalytic oxidation of 4-chlorophenol and dichloroacetate in nitrated Pt- TiO_2 aqueous suspensions. *J Photochem Photobiol A* 203:145–150
- Trari M, Bouguelia A, Bessekhoud Y (2006) *p*-Type CuYO_2 as hydrogen photocathode. *Sol Energy Mater Sol Cell* 90:190–202
- Yaron P (2010) Application of TiO_2 photocatalysis for air treatment: patents' overview. *Appl Catal B Environ* 99:448–460